J|A|C|S
ARTICLES
Published on Web 10/10/2007

Anatase-TiO_2 Nanomaterials: Analysis of Key Parameters Controlling Crystallization

Marcos Fernández-García,*,† Carolina Belver,† Jonathan C. Hanson,‡ Xianqin Wang,‡ and José A. Rodriguez‡

Contribution from the Instituto de Catálisis y Petroleoquímica, CSIC, C/Marie Curie 2, Cantoblanco, 28049-Madrid, Spain, and Department of Chemistry, Brookhaven National Laboratory, Upton, New York 11973

Received June 5, 2007; E-mail: m.fernandez@icp.csic.es

Abstract: Nanoparticulated TiO_2 materials with anatase structure were synthesized by using a microemulsion method. The structural characteristics of the amorphous solid precursors and their evolution during thermal treatments were studied by using X-ray absorption structure (X-ray absorption near edge structure XANES and extended X-ray absorption fine structure EXAFS), XRD-PDF (X-ray diffraction-pair distribution function), and infrared spectroscopy. Concerning the precursor materials, XANES and EXAFS showed a local order closely related to that of the anatase structure but containing defective, undercoordinated Ti_{5c}^{4+} species in addition to normal Ti_{6c}^{4+} species. The PDF technique detects differences among samples in the local order (below 1 nm) and showed that primary particle size varies throughout the amorphous precursor series. The physical interpretation of results concerning the amorphous materials and their evolution under thermal treatment gives conclusive evidence that local, intraparticle ordering variations determine the temperature for the onset of the nucleation process and drive the solid behavior through the whole crystallization process. The significance of this result in the context of current crystallization theories of oxide-based nanocrystalline solids is discussed.

1. Introduction

Titanium dioxide (TiO_2) is one of the most prominent oxide materials for performing various kinds of industrial applications related to catalysis among which the selective reduction of NO*x* in stationary sources[1,2] and photocatalysis for pollutant elimination[3] or organic synthesis[4] appear as rather important. Additional applications include its use as a white pigment in paintings,[5] as part of photovoltaic devices[6] and sensors,[7] as a food additive,[8] in cosmetics[9] and as a potential tool in cancer treatment.[10] Experimental approaches to scale down the TiO_2 primary particle size to the nanometer scale are now actively investigated in order to improve its current applications in sensor or catalysis fields and to reach more advanced ones like its use in electrochromic devices.[11] As a general result, the nanostructure induces an increase of surface area by the corresponding decrease of the primary particle size with concomitant potential enhancement of the chemical activity (connected with several structural and electronic size-related effects) and also of the photochemical/photophysical activities by reduction of light scattering.[12] In TiO_2 materials, the so-called "quantum-confinement" or "quantum-size effect" is restricted to very low sizes, below 10 nm, due to their rather low exciton Bohr radii. This would mean that a significant part of the potential novel chemical or physical applications needs to be carefully explored in the range of a few nanometers.[12−14]

Anatase, rutile, and brookite are the most common polymorphs of titania (TiO_2). Anatase is the dominant outcome of the vast majority of liquid−solid and gas−solid transformation-based preparation methods.[15,16] This is a consequence of being a stable polymorph at working temperatures for sizes (e.g., primary particle size) below ca. 15 nm.[17,18] However, samples often contain some brookite as an impurity (in low percentage) or, alternatively, mixtures of anatase and rutile, as the presence of impurities or phase mixture variables are adjusted or

† CSIC.
‡ Brookhaven National Laboratory.

(1) Bosh, H.; Janssen, F. *Catal. Today* **1988**, *2*, 369.
(2) Forzatti, P. *Catal. Today* **2000**, *62*, 51.
(3) Hoffman, M. R.; Martin, S. T.; Choi, W.; Bahneman, D. W. *Chem. Rev.* **1995**, *95*, 69.
(4) Maldoti, A.; Molinari, A.; Amadeni, R. *Chem. Rev.* **2002**, *102*, 3811.
(5) Johnson, R. W.; Thieles, E. S.; French, R. H. *Tappi. J.* **1997**, *80*, 233.
(6) Kalyanasendevan, K.; Gratzel, M. in *Optoelectronics Properties of Inorganic Compounds*; Roundhill, D. M., Fackler, J. P., Eds.; Plenum: New York, 1999; pp 169−194.
(7) Sheveglieri, G., Ed. *Gas sensors*; Kluwer: Dordrecht, 1992.
(8) Phillips, L. G.; Barbeno, D. M. *J. Dairy Sci.* **1997**, *80*, 2726.
(9) Selhofer, H. *Vacuum Thin Films* (August, 1999) 15.
(10) Fujishima, A.; Rao, T. N.; Tryk, D. A. *J. Photochem. Photobiol. C* **2000**, *1*, 1.
(11) Bonhole, P.; Gogniat, E.; Gratzel, M.; Ashrit, P. V. *Thin Solid Films* **1999**, *350*, 269.
(12) Fernández-García, M.; Martínez-Arias, A.; Hanson J. C.; Rodriguez, J. A. *Chem. Rev.* **2004**, *104*, 4063.
(13) Zhang, H.-J.; Wang, L.-S. *J. Am. Chem. Soc.* **2007**, *129*, 3022.
(14) Borello, E.; Lamberti, C.; Bordigas, S.; Zecchina, A.; Otero-Arean, C. *Appl. Phys. Lett.* **1997**, *71*, 2319.
(15) *Synthesis, Properties and Applications of Solid Oxides*; Rodríguez, J. A., Fernández-García, M., Eds.; John Wiley: New York, 2007; Chapters 4, 5, 20.
(16) Dietbold, U. *Surf. Sci. Rep.* **2003**, *48*, 53.
(17) Zhang, H.; Bandfield, J. F. *J. Mater. Chem.* **1998**, *8*, 2073.
(18) Hu, Y.; Tsai, H. L.; Hung, C. L. *Mater Sci. Eng. A* **2003**, *344*, 209.

10.1021/ja074064m CCC: $37.00

modulated by changing the preparation conditions (temperature, precursor concentration, etc.).[12,15,18]

As the majority of the practical applications of TiO_2 above-mentioned are linked to the anatase structure and this phase stability is in turn related to the primary particle size,[12,16,17] control of the nanostructure appears as a basic objective in the optimization of the industrial-oriented properties of anatase. Understanding the crystallization process of anatase from amorphous solid materials typically obtained at the initial synthesis step appears of prime importance in this context. In a more general view, results for titania are also important in that they elucidate the general way in which primary particle size can affect the behavior of oxide materials.

Upon heating, amorphous Ti-containing materials would transform on anatase.[12,15,16,19] Exarhos et al. were the first to study the kinetics of the corresponding transition of amorphous films supported on silica substrates.[19] Under hydrothermal conditions, several groups gave evidence of the media influence (pH, presence of ions) on the crystallization mechanism and pointed out that the rate-determining step can be related to the incorporation of new building units at the surface of the growing anatase crystal (solid-type step) and/or the dissolution of small anatase particles (Ostwald ripening; liquid-type step).[20−23] In other studies, using sol−gel[24,25] or microemulsion[26] procedures, details of the solid-state transformation mechanism leading to the anatase phase have been reported. Quantitative analysis of the key kinetic parameters controlling the amorphous titania to anatase transformation has been attempted in liquid media under hydrothermal conditions[21] and for solid−solid transformations concerning titania films,[19] powders,[25,26] or mesostructured[27] systems. The physical characteristics of the transformation (e.g., onset and reaction rate − energy of activation) in air should be different from those in liquid media as, obviously, dissolution steps are critically involved in the latter. The broad range of temperatures where amorphous titania solids transform into anatase (see below) also tells of a wide range of situations within the air-assisted transformation occurring in solid materials. In fact, crystallization has been considered to be controlled by either surface[19,26,27] or interface[25] nucleation processes. The subsequent step, e.g., growth of the anatase particles, is of lesser importance although fine works have been devoted to its study.[28] As a first approach to the rationalization of the nucleation mechanism, one may expect that interface nucleation can work at low temperature, starting from the lowest onset published (ca. 350 °C), while the surface dominated mechanism may get primacy above a certain temperature, ca. 600 °C.[29] However, a point to stress is that all the above analyses are mainly of kinetic nature and always involve several assumptions to establish the kinetic mechanism, which is ultimately validated by a multi-parameter fitting procedure of the experimental data. The assumptions are therefore inherent to the mechanism and are only self-consistently proven by fitting; consequently, they may drive misleading interpretations.

Table 1. Water/Titanium Molar (R) and Water/Surfactant Molar (ω) Ratios Used during the Microemulsion Synthesis of Ti-containing Solids

sample	ω	R
T	18	110
Tw	18	110
TA	4.5	220
TB	3	220
TwB	3	220

In this work we examined the crystallization of anatase from amorphous titania powders using an essentially assumption-free experimental approach. Using bulk and surface structural characterization techniques sensitive to both local and long range order, we will prove that the anatase nucleation onset is exclusively dependent on amorphous intraparticle structural characteristics and then that anatase crystallization is essentially free of interface interferences. It will be shown that this occurs with samples crystallizing in the 400 to 600 °C temperature interval, indicating the invariance of the mechanism with temperature. We will also show that the structural characteristics of the initial, amorphous powders determine the final morphology of the anatase nanoparticles, inferring in this manner the main parameters of the growth step.

2. Experimental Section

Preparation of the TiO_2 Oxide Precursors. Ti−O precursor materials were prepared using a microemulsion synthetic route by addition of titanium(IV) isopropoxide (Aldrich) to an inverse emulsion containing an aqueous phase (50 mL) dispersed in *n*-heptane (85/10 v/v vs H_2O; Panreac) and using either Triton X-100 (variable quantity; Aldrich) or Tween 85 (variable quantity; Aldrich) as surfactant. In the case of Triton X-100 and following standard recipes, 1-hexanol (105/100 v/v vs surfactant; Aldrich) was utilized as a cosurfactant.[30] The resulting mixture was vigorously stirred for 24 h, centrifuged, decanted, rinsed under stirring five consecutive times with methanol (2), water (2), and acetone (1), in order to eliminate any portion from the organic and surfactant media, and dried at 110 °C for 24 h. Sample labels are T, TA, and TB for Triton-derived materials and Tw and TwB for Tween-derived ones. The main synthesis details are summarized in Table 1.

Characterization Experiments. The Ti K-edge X-ray absorption near edge structure (XANES) and extended X-ray absorption fine structure (EXAFS) spectra of Ti−O amorphous precursor materials were collected at the NSLS on beamline X19A in the "fluorescence-yield mode" using a double-Si(111) crystal fixed-exit monochromator with feedback on the second crystal and a special cell with a modified PIPS detector.[32] XAS experiments were conducted in a fluorescence mode due to the experimental problems encountered in preparing thin samples to allow transmission experiments. All the XANES spectra were taken using a constant scan step of 0.5 eV through the edge region, and the energy resolution was close to 0.4−0.7 eV. Energy calibration was performed with the help of a Ti foil and spectra normalization by giving a value of 1 to the atomic-like background contribution at 30 eV from

(19) Exarhos, G. J.; Aloi, M. *Thin Solid Films* **1990**, *193*, 42.
(20) Yanagisawa, K; Ovenstone, J.. *J. Phys. Chem. B* **1999**, *103*, 7781.
(21) Inoue, Y.; Yin, S.; Uchida, S.; Fujishiro, Y.; Ishitsura, M.; Min, E.; Sato, T. *Br. Ceram. Trans.* **1998**, *97*, 222.
(22) Yin, H.; Wadax, X.; Kitamura, T.; Kanbe, S.; Murasawa, S.; Mori, H.; Sakata, T.; Yamagida, T. *J. Mater. Chem.* **2001**, *11*, 1694.
(23) Testino, A.; Bellobono, I. R.; Buscaglia, V.; Canevali, C.; D'Arienzo, M.; Polizzi, S.; Scotti, R.; Morazzoni, F. *J. Am. Chem. Soc.* **2007**, *129*, 3564.
(24) Ohtani, B.; Ogawa, Y.; Wishimoto, S. *J. Phys. Chem. B* **1997**, *101*, 3746.
(25) Zhang, H.; Banfield, J. F. *Chem. Mater.* **2002**, *14*, 4145.
(26) Fernández-García, M.; Wang, X.; Belver, C.; Hanson, J. C.; Rodríguez, J. A. *J. Phys. Chem. C* **2007**, *111*, 674.
(27) Kirsch, B. L.; Richman, E. K.; Riley, A. E.; Tolbert, S. H. *J. Phys. Chem. B* **2004**, *108*, 12698.
(28) Li, G.; Li, L.; Boerio-Goates, J.; Woodfield, B. F. *J. Am. Chem. Soc.* **2005**, *127*, 8659.
(29) Zhang, H.; Banfield, J. F. *J. Phys. Chem. C* **2007**, *111*, 6621.
(30) Fuerte, A.; Hernández-Alonso, M. D.; Maira, A. J.; Martínez-Arias, A.; Fernández-García, M.; Conesa, J. C.; Soria, J.; Munuera, G. *J. Catal.* **2002**, *212*, 1.
(31) Klementev, K. V. *J. Phys. D: Appl. Phys.* **2001**, *34*, 209.
(32) Rodriguez, J. A.; Hanson, J. C.; Kim, J.-Y.; Liu, G.; Iglesias-Juez, A.; Fernández-García, M. *J. Phys. Chem. B* **2003**, *107*, 3535.

the edge. EXAFS spectra were taken using several regions with a constant k step (ca. 0.03 $Å^{-1}$) up to above 13 $Å^{-1}$. A bulk rutile reference was also obtained in fluorescence and transmission mode in order to correct for self-absorption phenomena. Ti−O/Ti−Ti phase and amplitude functions were extracted from bulk anatase-TiO_2/Ti materials. Fitting results were obtained by using the VIPER program (www.dessy.de/klmn/viper.html),[31] and error bars were estimated with k^1/k^3 weighted fittings. The number of free parameters allowed by the fitting k (2.95−11.9 $Å^{-1}$) and R (0.60−3.06 Å) ranges used is above 20 according to the Nyquist theorem ($N_{free} = 2\Delta k\Delta R/\pi + 1$).

The time-resolved X-ray diffraction (TR-XRD) data were collected at beamline X7B ($\lambda = 0.1653 \pm 0.0005$ Å) of the National Synchrotron Light Source (NSLS) at the Brookhaven National Laboratory (BNL). The wavelength calibration was determined with the FIT2D code based on the diffraction pattern for LaB_6.[32,33] In the TR-XRD experiments dealing with the thermal evolution of Ti−O nanomaterials, the sample (ca. 30 mg) was kept in a sapphire capillary and heated using a small resistance heater placed around the capillary from 25 to 900 °C under 5% O_2/He.[33] XRD patterns were taken at 20 °C intervals. A chromel−alumel thermocouple was used to measure the temperature of the sample. Two-dimensional powder patterns were collected with an MAR CCD 165 image plate detector, and the powder rings were integrated using the FIT2D code.[34] Average grain/particle domain sizes (D) were calculated from the most intense diffraction peak (101) using the Scherrer formula.[35]

X-ray patterns for pair distribution function (PDF) analysis were obtained at the ID11 line ($\lambda = 0.1370 \pm 0.0005$ Å) of the Advanced Photon Source (APS) at the Argonne National Laboratory (ANL). Wavelength calibration and signal acquisition were done as above but using an Mar34 image plate as detector. Samples (ca. 30 mg) were placed in a quartz tube and heated from 25 to 700 °C under 5% O_2/He. The temperature change per image was 17 °C. The PDF analysis was performed with the PDFgetx program.[36] After background subtraction and normalization using atomic form factors and Compton scattering factors, the smooth atomic scattering contribution to the intensity is removed to produce the structure factors for each sample. The structure factors were subsequently multiplied by the q scattering axis and Fourier transformed to give real-space pair distributions (PDF). The use of high-energy X-rays allows access to high q values, revealing fine structure features differing by less than 0.2 Å.

Diffuse Reflectance Infrared Fourier Transform Spectra (DRIFTS) were taken in a Bruker Equinox 55 FTIR spectrometer fitted with an MCT detector. The DRIFTS cell (Harrick) was fitted with CaF_2 windows and a heating cartridge that allowed samples to be heated to 700 °C. Samples of *ca*. 60 mg were dried *in situ* at 110 °C with synthetic air (20% O_2 in He) and ramped at 5 °C min^{-1} up to 700 °C. The spectra consisted of 100 accumulations with a total of 2 min of acquisition time, using a 4 cm^{-1} resolution.

3. Results and Discussion

Precursor Materials. The chemical nature and structural characteristics of the amorphous titania materials were analyzed using X-ray absorption spectroscopies (XASs). XANES spectra of the five amorphous precursors (Figure 1) show broad and featureless continuum resonances that clearly resemble those characteristic of the crystalline anatase-TiO_2 material. This indicates a fully oxidized Ti(IV) state for all samples. The XANES spectra contain pre-edge features ascribable to the dipole 1s → 3d transition; the peak shape shows a prominent contribution at ca. 4970.5 eV, on top of a structure (e.g., three resolved peaks) characteristic of six-coordinated (Ti_{6c}^{4+}) cations located on the anatase-TiO_2 structure (see the well crystallized reference included in Figure 1). The 4970.5 eV peak gives evidence of the presence of five-coordinated (Ti_{5c}^{4+}) cations.[12,37−39] Thus, the XANES analysis and, particularly, the pre-edge features allow us to conclude that the local environment in our Ti−O precursors contains a mixture of Ti_{5c}^{4+}/Ti_{6c}^{4+} cation species within an anatase-type local order.[12,40] No apparent differences are encountered among the precursor materials. To better define the close environment of Ti/O ions we will use EXAFS (Figure 2) and PDF (Figure 3). In Figure 2 we compare Ti K-edge EXAFS Fourier transforms for samples obtained using the same ω/R preparation variables but obtained using different surfactants. Numerical analysis gives two Ti−O shells at 1.72−1.75 and 1.90−1.92 Å and a Ti−Ti contribution at 3.02−3.06 Å (phase corrected distances; Table 2). The intensities of the Ti−O shells appear higher than that corresponding to well-crystallized anatase, but a strong intensity decrease can be observed at higher R values, being only possible to quantitatively analyze the next Ti−Ti shell. Significant differences among amorphous precursor materials only concern the Ti−Ti coordination numbers (CNs), which is 2.1 ± 0.4 for samples of the "T" series (T, TA, TB) and seem a little higher for TwB (2.6 ± 0.3). As the crystalline anatase structure has a Ti−Ti CN of 4, this would mean that Ti cations have a severely restricted tridimensional (3D) connectivity for all samples. In fact, a CN of 2 is evidence of a −Ti−O−Ti−O−Ti− chainlike cation−cation connectivity. Only the TwB sample seems to display a CN higher than 2, indicating a better defined local order with respect to the remaining precursor samples.

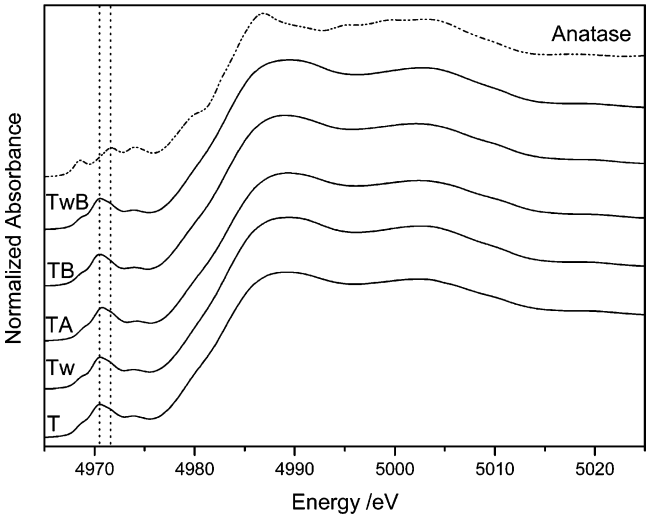

Figure 1. XANES spectra of precursor materials and a well-crystallized anatase reference.

Further structural information can be extracted from the ("more sensitive" to longer ranger order) PDF profiles displayed in Figure 3. The PDF signal takes into account all components of the XRD pattern, e.g., both the sharper Bragg-like and the diffuse-like features, and contains all characteristic interatomic

(33) (a) Norby P.; Hanson, J. *Catal. Today*, **1998**, *39*, 301 and references therein. (b) Chupas, P. J.; Ciraolo, M. F.; Hanson, J. C.; Grey, C. P. *J. Am. Chem. Soc.* **2001**, *123*, 1694.
(34) Hammersely, A. P.; Svensson, S. O.; Thompson, A. *Nucl. Instrum. Methods Phys. Res.* **1994**, *346*, 321.
(35) Snyder, R. L.; Fiala, J.; Bunge, H. J. *Defects and Microstructure Analysis by Diffraction*; Oxford University Press: New York, 1999.
(36) Qui, X.; Thompson, J. W.; Billinge, S. J. L. *J. Appl. Crystallogr*. **2004**, *37*, 678.
(37) Farges, F.; Brown, G. E., Jr.; Rehr, J. J. *Phys. Rev. B* **1997**, *56*, 1809.
(38) Luca, V.; Djajanti, S.; Howe, R. F. *J. Phys. Chem. B* **1998**, *102*, 10650.
(39) Pertipino, C.; Solari, P. L.; Lamberti, C. *J. Phys. Chem. B* **2005**, *109*, 13132.
(40) Wu, Z. Y.; Ouvard, G.; Gressier, P.; Natoli, C. R. *Phys. Rev. B* **1997**, *55*, 10382.

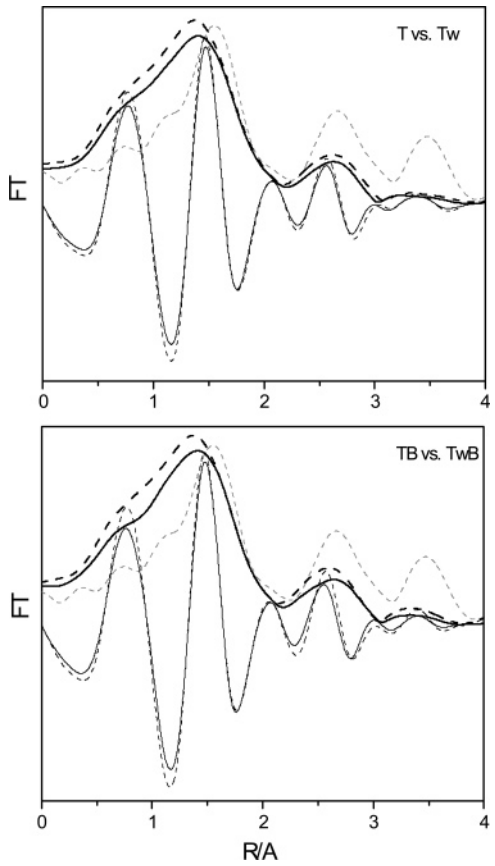

Figure 2. Fourier transforms of k^2-weighted EXAFS spectra of precursor materials ("T" samples, full line; "Tw" samples, dashed line) and a well-crystallized anatase reference (gray line).

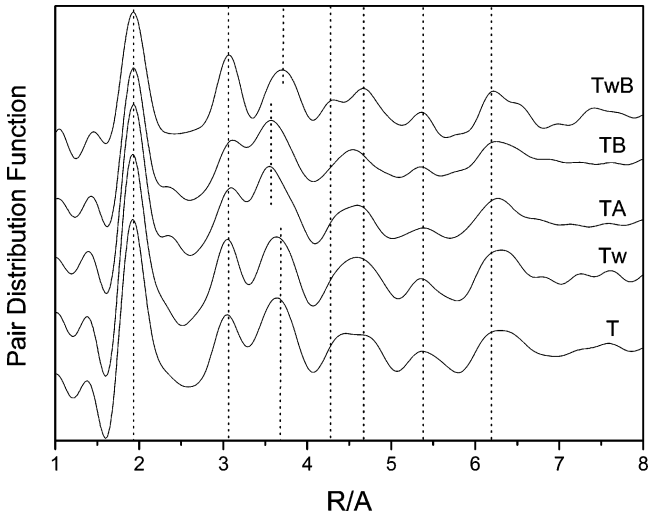

Figure 3. Real-space pair distribution functions (PDF) of the precursor materials at room temperature.

distances in the material, the shortest bond length producing the first peak. In nanoparticles, the maximum interatomic distance that can contribute to the PDF is limited by the particle diameter. Although interatomic scattering may occur between atoms in different particles, the nanoparticles are on average not aligned, interparticle events thus averaging to zero.[41] In good agreement with EXAFS, we may see that atom−atom bond distances are best defined in the TwB material among our precursors. This is indicative of a better local to medium range order. Two main differences are detected in the PDFs; the first concerns distances between 3 and 4 Å. In this region, TA/TB samples shows an enhanced overlapping among peaks and a decreased distance for the contribution peaking near the higher end. The second point takes into account the differences in intensity. Diffraction measurements on nanoparticles are sensitive to both particle size and disorder, both of which cause diffraction peak broadening. The lower height and larger peak widths for samples "B" (TB, but particularly, TwB) clearly indicate an effect related to the particle size of the corresponding amorphous materials, which seems lower than that obtained for the rest of the samples. Apart from the above-mentioned differences we do not detect any differential behavior among the precursor materials; this accounts for the first Ti−O and O−O shells located below 3 Å and for all characteristic interatomic distances above 4 Å, although, as mentioned, the better defined signal of the TwB sample becomes evident.

Thus, from a structural point of view, the multitechnique XAS/PDF approach provides evidence of a limited Ti−O−Ti connectivity with a shortening of the first, highly disordered Ti−O distance detected by EXAFS. This may be related to the presence of (a reasonably minor contribution of) Ti_{5c}^{4+} undercoordinated cations while, according to PDF, Ti_{6c}^{4+} cations display a distance characteristic of TiO_6 octahedra units (ca. 1.9 Å), similarly as those detected in the three most common crystalline polymorphs of titania (anatase, rutile, brookite). The TwB sample is the only one having an incipient 3D-like order with significant differences with the other samples. Overall, XANES and EXAFS showed a local order closely related to that of the anatase structure, discarding any type of local order related to other titania polymorphs (rutile, brookite), reduced oxides, and/or oxo-hydroxides.[12] The PDF technique allows us to analyze local and middle range order in a more insightful way, discerning that there are significant differences in the local ordering in the 3−4 Å interval. So, the connectivity of TiO_6

Table 2. Ti K-Edge EXAFS Fitting Results for Ti-Containing Precursor Materials

shell	*N*	*R*/Å	$\Delta\sigma/10^3 \times$ Å^2	ΔE_0/eV
		T; 7.7%[a]		
Ti−O	$1.2_5 \pm 0.3_5$	1.72 ± 0.02	10.1 ± 0.4	−6.91
Ti−O	5.1 ± 0.6	1.91 ± 0.01	7.5 ± 0.7	−6.01
Ti−Ti	1.9 ± 0.3	3.02 ± 0.01	2.0 ± 0.6	-8.01_5
		Tw; 8.9%		
Ti−O	$1.4_5 \pm 0.4$	1.73 ± 0.02	9.0 ± 0.5	−7.41
Ti−O	5.3 ± 0.7	1.90 ± 0.01	8.5 ± 0.6	−5.51
Ti−Ti	2.2 ± 0.3	3.03 ± 0.01	1.7 ± 0.6	-7.01_5
		TA, 11.1%		
Ti−O	$1.2_5 \pm 0.3_5$	1.72 ± 0.02	9.5 ± 0.3	−5.21
Ti−O	5.0 ± 0.7	1.90 ± 0.01	7.0 ± 0.7	−6.91
Ti−Ti	$2.3 \pm 0.3_5$	3.04 ± 0.01	1.5 ± 0.8	-6.01_5
		TB; 8.7%		
Ti−O	1.3 ± 0.3	1.72 ± 0.02	9.0 ± 0.3	−7.51
Ti−O	5.1 ± 0.7	1.90 ± 0.01	7.0 ± 0.5	−6.01
Ti−Ti	2.2 ± 0.3	3.02 ± 0.01	2.4 ± 0.8	-5.01_5
		TwB; 5.7%		
Ti−O	$1.4 \pm 0.3_5$	1.74 ± 0.02	9.1 ± 0.4	−7.21
Ti−O	5.3 ± 0.7	1.92 ± 0.01	8.0 ± 0.4	−6.91
Ti−Ti	2.6 ± 0.3	3.05 ± 0.01	1.0 ± 0.9	-7.01_5

[a] Sample label followed by fitting factor $R(\%) = (\int [\chi^T - \chi^E]k^2\, dk / [\chi^E]k^2\, dk) \times 100\%$: χ^T being the theoretically calculated EXAFS and χ^E being the EXAFS obtained via experiment.

(41) Egami, T. *Local structure from Diffraction*; Billinge, S. J. L., Thorpe, M. F., Eds.; Plenum: New York, 1998.

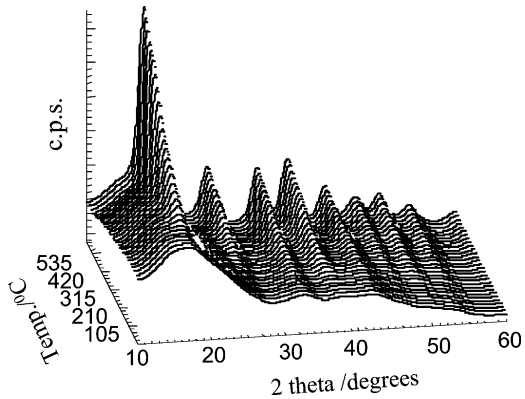

Figure 4. WAXS/XRD diffractograms of the T sample during a heating treatment under dry air.

(Ti_{6c}^{4+} cations) and TiO_5 (Ti_{5c}^{4+} cations) units seems variable among the precursor samples. The relevance of this point will be unveiled in the following section. The PDF analysis also showed that TB/TwB amorphous materials have a lower primary particle size with respect to the rest of the solids.

Structural Factors on Anatase Genesis. The thermal evolution of the initially amorphous materials under an O_2/He atmosphere was investigated using a multitechnique approach. Figure 4 depicts the diffraction raw data evolution for sample T as a representative example of what can be obtained using this technique. The amorphous structure of the initial material, which mainly leads to broad, diffuse-like features in the XRD pattern, develops on a well-crystallized anatase nanostructure displaying Bragg-like peaks during thermal evolution. An absence of signals related to any other phase (e.g., brookite and/or rutile) of titania throughout the whole thermal treatment is noticed in Figure 4. This was unequivocally proven for all materials in the PD functions (extracted from diffraction data) plotted in Figure 5 and further confirmed using XANES (not shown).

A point of relevance of the PDF study concerns the temperature of nucleation of the anatase structure. A gray color is used in Figure 5 to highlight the spectrum where the well-defined structure of anatase starts to appear, highlighting in this way the nucleation onset temperature. A complementary view of this process is obtained by following the (101) peak of anatase (JPDS 21-1272) as displayed in Figure 6. Using both views (Figures 5 and 6) we see two different behaviors. While samples T, Tw, and TwB nucleate around 350−400 °C, samples TA and TB nucleate around/above 550 °C. Note that the onset does not display a behavior related with the particle size of the amorphous materials and/or the middle-long range order, as, in the first case two groups of samples containing T/Tw/TA vs TB/TwB could be expected while, in the second, only the TwB sample appears to have a reasonably better defined order/atom connectivity above ca. 5 Å. On the contrary, the nucleation onset temperature is clearly related to the local-middle range order of materials, as shown by the significant differences among samples highlighted in the 3−4 Å interval (Figures 3 and 5). This local-middle range ordering correctly sorts out the amorphous solids in two groups, T/Tw/TwB vs TA/TB, paralleling the onset behavior depicted in Figure 6. So, key differences among samples appear related to the atom connectivity between the Ti−Ti first coordination distance and subsequent Ti−O and Ti−Ti shells (see Figure 5). This, as mentioned, concerns the connectivity of TiO_6/ TiO_5 units.

A graphical view of the structural configuration is depicted in Figure 7. This figure shows atoms inside the anatase unit cell and those of interest of contiguous cells along the *a* cell parameter direction. As XAS/PDF indicate the close order of amorphous materials to that of anatase, the pictorial view given in Figure 7 may serve as a reasonable (local) description for both situations. Around the central atom of Ti (labeled as "0"), we numbered atoms corresponding to the first Ti−Ti distance at 3.02−3.06 Å as 1 while atoms corresponding to shells ahead are numbered as 2 (Ti−Ti; 3.78 Å in crystalline anatase), 3 (Ti−O; 3.86 Å in anatase), and 4 (Ti−Ti; 4.85 Å in anatase). The Ti−O shell at 4.25 Å (in anatase) is not marked for the sake of clarity. In all cases, differences between amorphous materials and the well-crystallized anatase structure are evidenced by comparison between the first and last PDF profile (i.e., near room temperature/highest temperature) included in Figure 5. Shells 1 to 3 of Figure 7 are those contributing to the 3−4 Å interval of the PDF signals plotted in Figure 5. In the amorphous materials we can see the strong overlapping of peaks for TA/TB (Figure 5C,D), which is less dramatic for the remaining samples. With respect to anatase, a slightly larger Ti−Ti distance at ca. 3.05−3.07 Å (shell 1; Figure 7) but significantly distorted Ti−Ti,O distances (2/3/4 shells in Figure 7) are observed. The average position of these last Ti−Ti,O peak(s) in the initial amorphous materials is however dependent on the sample; T, Tw, and TwB materials display maxima around 3.7 Å, a position somewhat inferior to the 3.78 Å characteristic of anatase in the well crystallized reference spectra. This shortening could be expected for a certainly more dense local packing that appears intermediate between those of rutile (3.58 Å) and anatase (3.78 Å).[12] A more dense local atomic arrangement may balance the energy loss coming from long-range electrostatics (e.g., Madelung potential). More importantly, TA and TB amorphous samples contain this Ti−Ti,O contribution at significantly lower distances, ca. 3.55 Å (Figure 5C,D).

From Figure 7, it becomes evident the interpretation of the structural differences encountered between our two types of initial amorphous materials. It appears that all samples display a more dense local packing arrangement than anatase but differ among themselves in the strong decrease of certain interatomic distances appearing in TA/TB. The local distribution of distances can be interpreted by a strong shrinking along the anatase *a* cell parameter direction together with a small elongation along the *c*-axis direction. The packing density appears radius dependent, losing density toward the surface; therefore, the above-mentioned shrinking effect is smoothed as the distance from the center of the amorphous particle increases. Still, softer replicas of the structural effects described above in the 3−4 Å interval are visible around 5 Å (Ti−Ti contributions at about 5.3−5.4 Å) in the temperature treatments depicted in Figure 5. Speaking from a local point of view and considering the TiO_6 as the building unit of the precursor materials, we can interpret the structural information in a simple way. Considering the Ti−Ti coordination numbers yielded by EXAFS and the PDF loss of signal well below 1 nm, we can end with an idealized model consisting of three TiO_6 units as seen in the center of Figure 7 (central Ti atom plus two Ti atoms marked as 1) and two additional units located above/below the first group of three

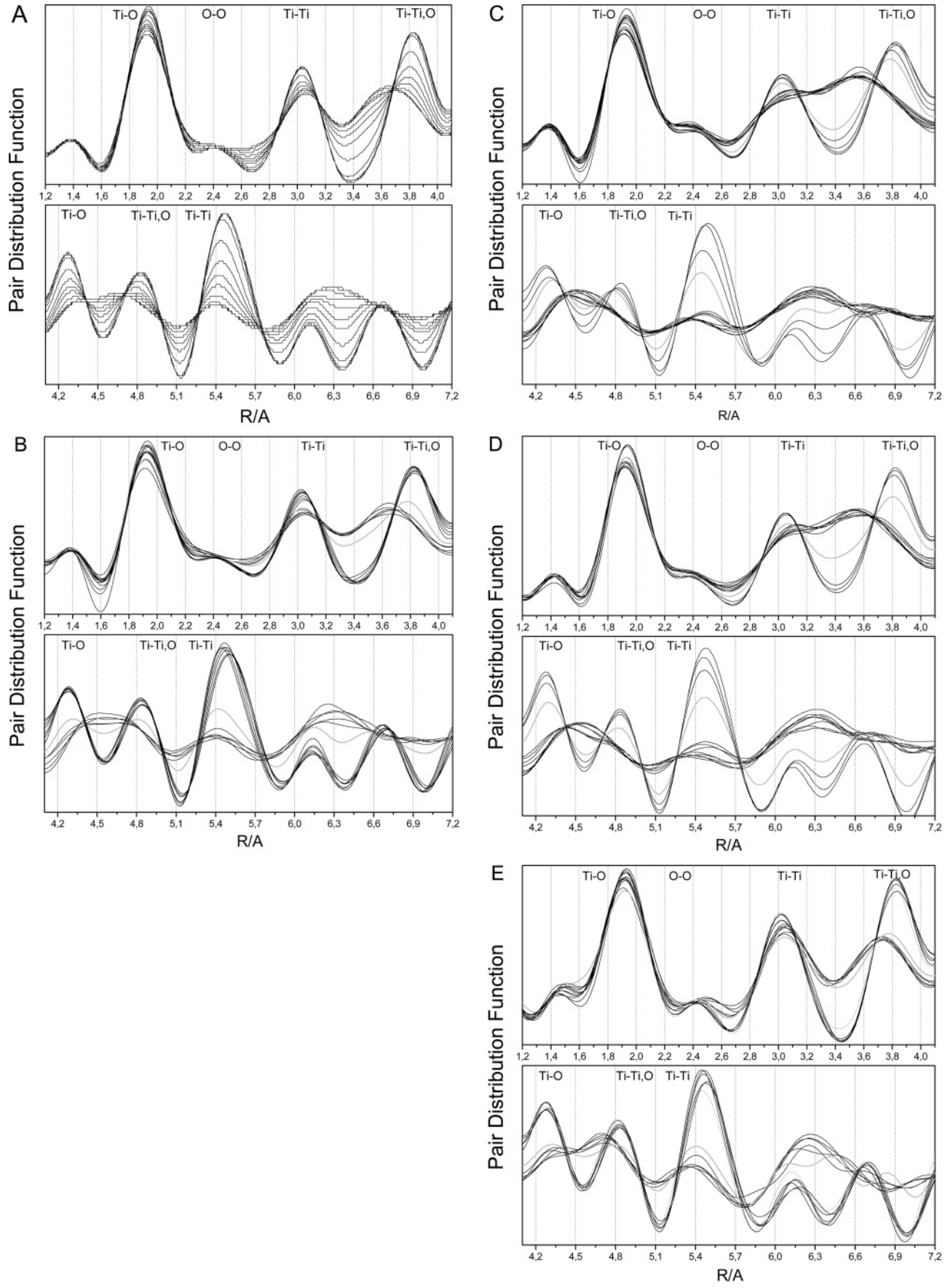

Figure 5. Real-space pair distribution functions (PDF) of the materials upon heating in dry air: (A) T, (B) Tw, (C) TA, (D) TB, and (E) TwB materials. Spectra are shown from 50 °C in steps of 50 °C. Labels indicate atomic nature of the shells contributing to the structure.

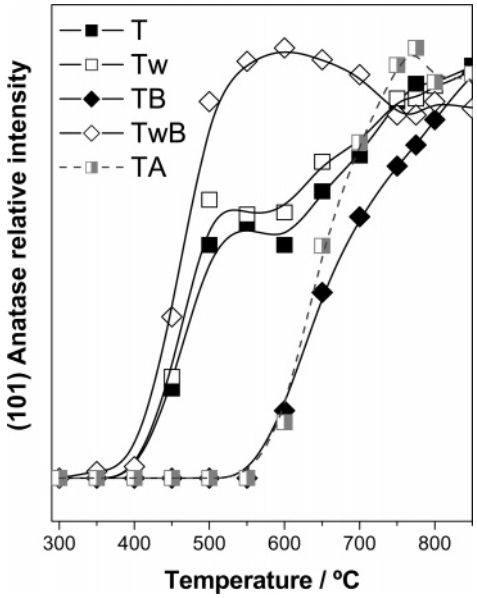

Figure 6. Normalized intensity of the (101) anatase reflection of Ti-containing materials as a function of the temperature of the heating treatment in dry air.

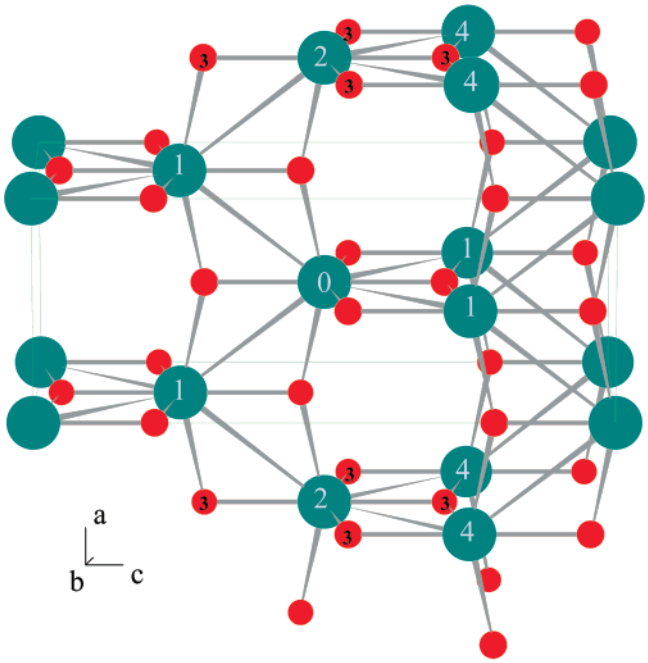

Figure 7. Schematic view of atoms located inside the anatase unit cell and selected atoms of contiguous cells along the *a*-axis. See text for details.

(Ti center atoms labeled as 2 in Figure 7). We can thus see that the anatase-type stacking of TiO_6 units is essentially held within the short length scale (below 1 nm), with a marked shortening along the *a*-axis but roughly maintaining the characteristic distance (projections) along the *b* and *c* axes. This would mean that we have an essentially 2D anatase-like structure (the local view takes into account the three TiO_6 units above-mentioned) with a third dimension having a significant compression ratio, which appears variable among amorphous precursors. We may speculate that defective Ti_{5c}^{4+} cations are preferentially located out of the anatase-type 2D structure, e.g., above and/or below such a planar structure.

Overall, the PDF analysis gives conclusive evidence that anatase nucleation is driven by intraparticle structural properties of the amorphous materials. From a local view we describe this as a different 3D stacking of TiO_6/TiO_5 units. The more dense atomic packing and concomitant shortening along the *a*-axis direction, the higher the onset of the nucleation process. A direct link is thus established between the local order characteristics of the precursor material and its stability and thermal evolution into a crystalline material. As a consequence, models that describe the onset step of the crystallization in terms of interface events on contact areas of the amorphous materials are not well grounded.[25] Due to the limited primary particle size of the amorphous materials and the possible preferential nucleation through the more dense planes (e.g., perpendicular to the anatase-like 2D structure), a surface-type (1D dimension-restricted) nucleation mechanism appears compatible with our results.[19,26,27]

For further progress on the rationalization of the crystallization mechanism, we will follow the nucleation and growth steps using infrared (IR) spectroscopy. The main aim of this study is the analysis of surface morphologies of the samples during the temperature ramp, following in this way both the amorphous state and the crystalline anatase phase. Recent density functional theory (DFT) and IR spectroscopy studies made available the accurate prediction of surface morphologies.[42] Such correlation is based on the O−H stretching frequencies of surface-adsorbed entities/molecules which only gives information at a local level.[43−45] This approach has advantages over microscopy and other studies as it can follow the process easily when the amorphous material is present. Panels A−E in Figure 8 present results for, respectively, T, Tw, TA, TB, and TwB precursor materials in the O−H region. Below the nucleation onset temperature, our amorphous precursors have OH-containing groups located on anatase-type (101)-terminated (3650−3660 cm^{-1}) and (100)-terminated (3709−3712 cm^{-1}) local environments. Additional peaks at ca. 3745−3750 (small) and 3620−3630 (tailing contribution) cm^{-1} reflect, respectively, (001)- and (101)-type local terminations[42−44] and are only easily discerned in the case of the TA/TB samples. While (101)-type terminations are always observed in the amorphous materials (Figure 8), (100)-type terminations are only detected when the temperature raises about 300 °C (T, Tw, TwB) or ca. 450 °C (TA, TB). Other contributions having less intensity like the (001)-type terminations, observed for TA/TB samples, parallel the behavior of the (100)-type signal. These observations highlight the fact that anatase-type surface terminations are formed well below the nucleation onset, originally developing the more stable (101)-surface termination,[16,46] followed by the (100)- and, for TA/TB samples, (001)-type surface terminations. The energy stability increase derived from the shrinking along the *a* spatial direction due to the initial more dense close packing leads to a more even growth along the three spatial directions during crystallization, ending in this way in highly isotropic (spherical) particles for samples TA and TB. Such particles present (101)/

(42) Dzwigaj, S.; Arrouvel, C.; Breysse, M.; Geantet, C.; Inoue, S.; Toulhoat, H.; Raybaud, P. *J. Catal.* **2005**, *236*, 245.
(43) Digne, M.; Sautet, P.; Breysse, M.; Touthoat, H. *J. Catal.* **2002**, *211*, 1.
(44) Digne, M.; Sautet, P.; Raybaud, P.; Euzen, P.; Touthoat, H. *J. Catal.* **2004**, *226*, 54.
(45) Usseglio, S.; Calza, P.; Damin, A.; Minero, C.; Bordiga, S.; Lamberti, C.; Pelezetti, E.; Zecchina, A. *Chem. Mater.* **2006**, *18*, 3412.
(46) Barnard, A. S.; Zapol, P.; Curtiss, L. A. *Surf. Sci.* **2005**, *582*, 2173.

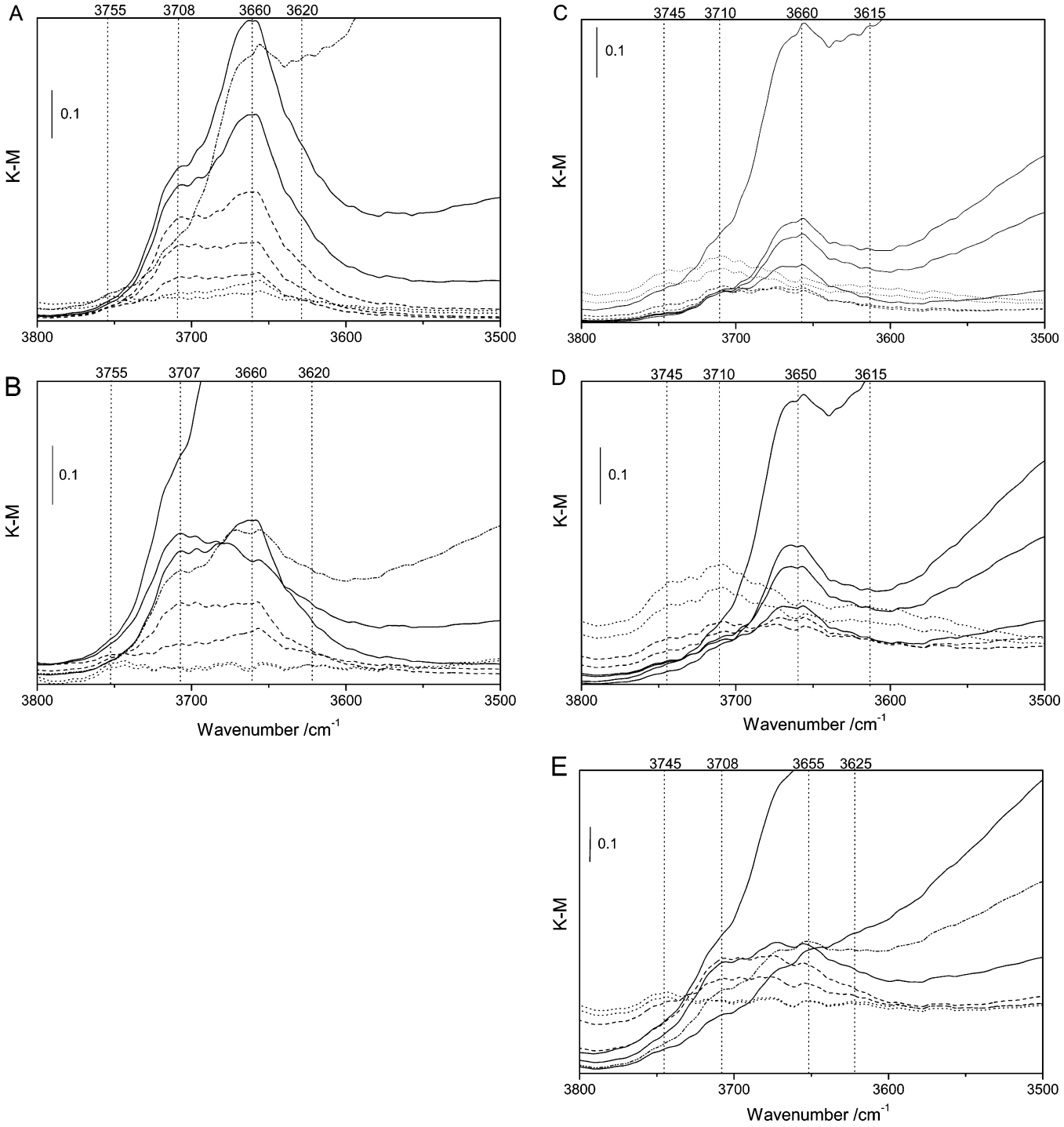

Figure 8. DRIFTS spectra of T (A), Tw (B), TA (C), TB (D), and TwB (E) materials recorded at 200, 300, 350, 400, 450, 500, 550, and 600 °C. See text for details.

(100)/(001)-type surface terminations in roughly similar proportions.[43,44] In the case of T, Tw, and TwB samples, the less compact atomic arrangement allows the predicted preferential growth along the *c*-axis direction and the preferential formation of the thermodynamically more stable surface (101).[16,46,47] As shown by using IR,[26,42,43] this preferential growth ended with elongated shapes (along the *c*-axis) which mainly exposed (101)/(100) surfaces. The dominance of the structural intraparticle variables of the amorphous precursor materials in the whole crystallization process is a consequence of the fact that nucleation is the rate-determining step, as particle growth is of much lesser importance.[19,21,25−27] So, final morphologies obtained after calcination mostly reflect the dominance of intraparticle structural parameters of the amorphous precursors.

4. Conclusions

This paper analyzed nanoparticulated TiO_2 materials with an anatase structure synthesized using a microemulsion method. Five amorphous precursor materials were analyzed by a combination of XAS, PDF-XRD, and IR spectroscopies. For all initial precursor meterials, XANES and EXAFS showed a local order closely related to that of the anatase structure but

(47) Barnard, A. S.; Curtiss, L. A. *Nano Lett.* **2005**, *5*, 1261.

containing defective, undercoordinated Ti_{5c}^{4+} species in addition to normal Ti_{6c}^{4+} species. The PDF technique unveils however differences among samples related to the local order and shows that the TB/TwB samples have a lower primary particle size with respect to the rest of the solids. Local order differences can be viewed as differences in the stacking of TiO_6/TiO_5 units located above/below a plane with anatase 2D characteristics.

The physical interpretation of the structural characterization of the amorphous materials and their evolution under thermal treatment gives conclusive evidence that local, intraparticle ordering variations determine the temperature for the onset of the nucleation process, at least in the 400−600 °C interval. As there is no doubt that this step (e.g., nucleation) is the rate-determining step of the anatase crystallization,[19,21,25−27] the same physical phenomena are critical in the overall nucleation and growth process. Differences among our samples appear exclusively related to the packing density of atoms, which leads to main structural differences at 3−4 Å from the center of the amorphous particle, which smoothly and progressively spread out with the increase of the distance above 4 Å. No other structural phenomena, e.g., precursor particle size and/or interparticle contact of amorphous particles, thus seem of importance in the crystallization of the anatase phase. The study thus gives support to kinetic models based on 2D-restricted surface-like nucleation and does not support those based on interface nucleation, interpreting in this way the ultimate physicochemical bases of the crystallization mechanism for anatase materials.

Acknowledgment. Work at the "Instituto de Catálisis y Petroleoquímica (CSIC)" was done with financial support from CICYT (Project CT2004-03409/BQU). The research carried out at the Chemistry Department of Brookhaven National Laboratory was financed through Contract DE-AC02-98CH10886 with the U.S. Department of Energy (Division of Chemical Sciences). The NSLS is supported by the Divisions of Materials and Chemical Sciences of DOE. The work at beamline ID11 at APS was supported by the U.S. Department of Energy (Office of Basic Energy Sciences) under Contract No. DE-AC02-06CH11357. C.B. thanks the Spanish "Ministerio de Educación y Ciencia" for a contract from the "Juan de la Cierva" program. Dr. Zhong (NSLS; BNL) and Dr. P. Chupas (APS, ANL) are also thanked for their help during XRD measurements.

JA074064M